INTERNATIONAL JOURNAL FOR NUMERICAL METHODS IN FLUIDS
Int. J. Numer. Meth. Fluids 2002; **40**:1431–1460 (DOI: 10.1002/fld.425)

Large-eddy simulation of a bluff-body flow on unstructured grids

S. Camarri[1], M. V. Salvetti[2,*,†], B. Koobus[3] and A. Dervieux[4]

[1] *Dipartimento di Ingegneria Aerospaziale, Università di Pisa, Italy*
[2] *Dipartimento di Ingegneria Aerospaziale, Università di Pisa, Italy*
[3] *Département de mathématiques, Université Montpellier II, France*
[4] *INRIA Sophia Antipolis, France*

SUMMARY

Large-eddy simulations of the flow around a square cylinder on coarse unstructured grids are investigated. The numerical solver is based on a mixed finite-volume/finite-element formulation. A modified Roe scheme is employed for convective terms, together with the MUSCL method to increase the order of accuracy. An upwinding parameter, γ_s, directly controls the numerical diffusion, which is formed of fourth-order space derivatives. The eddy-viscosity Smagorinsky model and its dynamic version are used for the subgrid scale (SGS) terms in the LES equations. The effects of upwinding, and, in particular, the interaction between SGS and numerical dissipation, are studied by varying the value of γ_s. The sensitivity to grid inhomogeneity and to SGS modelling are also investigated. Results are compared to those obtained in other LES in the literature and to experimental data. Copyright © 2002 John Wiley & Sons, Ltd.

KEY WORDS: large-eddy simulation; unstructured grids; finite-element/finite-volume solver; upwinding; bluff bodies

1. INTRODUCTION

The numerical simulation of flows of engineering and industrial interest, characterized by high Reynolds numbers (Re) and complex geometry, generally requires turbulence modelling.

The numerical discretization of the Reynolds-averaged Navier–Stokes equations (RANS) is the most widely used approach in engineering applications at the moment. However, in this approach all information on turbulent fluctuations is contained in the closure model. Although several closure models have been proposed in the literature, each of them is known to give satisfactory results only for particular classes of problems and it is almost impossible to devise a model of general validity.

* Correspondence to: M. V. Salvetti, Dipartimento di Ingegneria Aerospaziale, Università di Pisa, Via Caruso, 56122 Pisa, Italy.
† E-mail: mv.salvetti@ing.unipi.it

Received April 2001
Revised 9 February 2002

Large-eddy simulation (LES), in which only the large scale motion is computed and the subgrid scales (SGS) are modelled, could be an effective tool for tackling complex engineering flows. The great advantage of this approach is the direct simulation of the large scales, which are the most interesting in engineering applications. Moreover, the smallest turbulent scales might be considered less dependent on the particular flow considered. Therefore, the formulation of closure models of general validity seems to be more plausible than for RANS.

Large-eddy simulation has been successfully used in the recent years to simulate different turbulent flows. However, up to now most of the simulations reported in the literature are limited to simple geometries and moderate Reynolds numbers. Moreover, some of the recommendations given in the literature for LES, i.e. highly resolved grids and high-order numerical schemes (see, for instance, References [1, 2]), are clearly difficult to respect in an industrial context.

As far as computational domain discretization is concerned, structured grids, classically used in LES, are not well suited, since they are extremely difficult to generate around complex geometry. Unstructured grids offer an effective alternative; however, few examples of LES on unstructured grids are reported in the literature [3–10]. Thus, the capabilities of the LES approach on this type of grids need to be investigated more systematically. In particular, unstructured grids for industrial applications are characterized by:

(p1) a much coarser resolution than that generally used in LES in the literature;
(p2) grid inhomogeneity, i.e. large elements near small ones;
(p3) high element stretching.

Moreover, the use of unstructured grids and the need to limit the computational costs usually lead to numerical schemes having the following characteristics:

(p4) accuracy not higher than second order, since high-order schemes are expensive for unstructured meshes;
(p5) co-located schemes (higher-order mixed FEM are again too expensive), thus requiring upwinding for stability.

Our main goal is to investigate whether large-eddy simulation, carried out with 'industrial' grids and numerics, could be an alternative to RANS methods, at least for those flows for which RANS are known to have difficulties, such as bluff-body flows. With this aim, large-eddy simulations of the flow around a square cylinder were carried out on unstructured grids having characteristics (p1) and (p2), with a second-order (p4) co-located (p5) numerical scheme.

The flow around an infinite square cylinder at $Re = 22\,000$, based on free-stream velocity and the length of the cylinder side, was selected here because, although the geometry is rather simple and the Reynolds number moderate, this test case is well suited for a first investigation of LES capabilities in the perspective of application to industrial problems. More specifically, it is known that statistical turbulence models, such as those used in the RANS approach, usually have difficulties in accurately predicting the flow around bluff bodies (see, for instance, Reference [11] for applications to the square-cylinder test case). Indeed, although few RANS models [12, 13] could give quite satisfactory results if used together with a very fine grid resolution, they generally give a too high dissipation and do not take into account 3D phenomena and this yields significant discrepancies with the experimental results. Moreover, as shown in Reference [11], results may be significantly sensitive to the

boundary conditions imposed for the turbulent quantities, that are sometimes difficult to be assigned, e.g. the turbulent dissipation rate ε at the inflow. Conversely, since large-scale eddy structures dominate turbulent transport and since unsteady processes like vortex shedding are the prevailing features, then large-eddy simulation seems to be particularly well suited. Finally, the flow considered was one of the selected test cases in a workshop held in June 1995 in Germany and the results obtained in large-eddy simulations by different contributors are published and compared to experimental data in Reference [14]. More recent LES results are also documented in References [15, 16].

Since one of the main objectives of the present study is to investigate the capabilities of LES on coarse unstructured grids (point (p1)), the number of nodes used in the present simulations is significantly lower than in almost all the LES in References [14–16]. Grid coarseness is particularly critical near solid walls, and approximate boundary conditions are thus needed. In the present study, a near wall treatment classically used in RANS simulations was employed, together with the Reichardt wall law [17]. Most of the simulations in Reference [14] also use the same type of approximate boundary conditions, but with different wall laws. The Reichardt wall law has the advantage of describing the velocity profile not only in the logarithmic region of a turbulent boundary layer but also in the laminar sublayer and in the intermediate region. However, the derivation and validation of approximate boundary conditions in LES is certainly complex and still an unsolved problem; we thus preferred not to investigate this point in detail in this paper. In particular, our test case is not so sensitive to reasonable choices of boundary conditions at the solid walls, since laminar separation is fixed by the geometry. Rather, we plan to dedicate subsequent studies to this problem.

On coarse grids, the SGS model is expected to play a crucial role. Two SGS models are used in the present study. The first is the eddy-viscosity Smagorinsky model for compressible flows [18]. Although it is known to have several drawbacks, the simplicity of implementation and the low computational cost nevertheless render it attractive for industrial applications. Additional problems arise on unstructured grids, for instance the lack of theoretical work for definition of the equivalent filter width, needed to compute SGS viscosity. In the present paper we test a definition different from that generally used on unstructured grids in the literature [4, 5, 9, 10]. The second SGS model is the dynamic eddy-viscosity model [19], which is currently widely used in LES. The dynamic procedure is slightly modified here (as also done in References [6, 9]) to also evaluate the equivalent filter width and thereby overcome the indetermination in its definition. A local smoothing procedure is also proposed to avoid numerical instabilities due to large oscillations of the model coefficient.

As far as grid inhomogeneity is concerned (point (p2)), the results obtained on different grids having the same number of nodes but differently distributed are presented for both the Smagorinsky and dynamic SGS models. This allows us to study the sensitivity of LES results to local refinement obtained not by enrichment, but by modification of the node distribution and element shape, which is particularly easy to obtain for unstructured grids.

We do not address (p3) here, since it is anticipated that the numerical scheme employed is not well adapted to highly stretched meshes. Thus, in the grids used in the present study the elements are only moderately stretched.

The code employed [20], which has been developed for industrial problems, permits the simulation of compressible flows on unstructured grids. The spatial discretization is vertex centred to minimize the number of unknowns and is based on a mixed finite-volume/finite-element formulation. The Roe scheme [21], modified by the introduction of an upwinding

parameter γ_s [22], is used for the convective terms. The order of accuracy of the scheme is increased by the MUSCL reconstruction technique [23]. Either an implicit second-order accurate algorithm or explicit time advancing can be used.

The use of low-order (second-order) schemes (p4) is still a controversial point in LES. Indeed, some a priori and a posteriori studies (see, for instance, References [1, 2]) indicate that high-order or spectral schemes are needed to obtain reliable results in LES. On the other hand, successful LES have been documented in the literature with second-order accurate schemes for a wide variety of flows (see, for instance, References [24–26]). It is clear that a second-order method can give results as accurate as a higher-order one, provided that the grid used is fine enough to give the same level of error. In this paper, we aim to show that this is not even necessary and that a second-order accurate scheme can be used, provided that the numerical dissipation aspect is mastered. We also wish to emphasize that accuracy better than second order on unstructured, or even structured non-uniform meshes, is difficult to obtain without a high complexity in approximation assembly and a particular effort in dissipation design. Recently, an example of a third-order Taylor–Galerkin scheme applicable to LES on unstructured grids has been proposed in Reference [27]. However, our approach is quite different from the one by Colin and Rudgyard [27] in that they propose to develop a new software *ab initio* while we explore methods for adapting existing CFD codes to LES. More specifically, they use a P_2 interpolation, that is not only very different from, but also significantly more expensive than today's industrial standard in compressible CFD. Moreover, stiff transonic or supersonic phenomena cannot be taken into account in the method proposed in Reference [27] without adding *ad hoc* shock capturing, while shock capturing ability, although not applied in our study, is a natural option of our technology.

In our opinion, the most critical point concerning the numerical scheme that we use is in fact the need for numerical dissipation (p5). In MUSCL schemes, the pressure, as well as the other flow parameters, is stabilized by the upwinding of the scheme. Since there are no SGS terms for the stabilization of pressure, there is a risk of obtaining an non-physical oscillatory behaviour of the pressure field if the numerical viscosity is too low. This is in particular a problem for singularities, such as the cylinder corners in the test case considered. Although there are some studies in the literature which claim that the numerical dissipation given by monotone flux treatments may be an accurate SGS model (see References [10, 28] for an application to unstructured grids), it is common opinion in the LES community that the numerical viscosity can interact with the SGS model and significantly deteriorate the results (see, for instance, References [29, 30]). Thus it appears that the effects of numerical dissipation and SGS models should be separated as far as possible. In almost all previous applications of LES to unstructured grids [3–10], numerical dissipation is achieved by second-order spatial derivatives, either through Petrov–Galerkin upwinding or TVD limiters. Our proposal in this paper is to use a MUSCL upwind scheme which involves a dissipation built as a fourth-order spatial derivative of the flow variables and no TVD limiters. Fourier analysis clearly shows that such a dissipation has a much more localized effect on high frequencies than stabilizations based on second-order derivatives. This makes it possible to reduce the interaction between numerical dissipation, which damps only the highest resolved frequencies, and SGS modelling, which should reproduce the effects of SGS scales on all resolved frequencies. The Taylor–Galerkin method in Reference [27] also involves fourth-order spatial differences as the main numerical dissipation term. However, since it relies on a Lax–Wendroff type time advancing, the involved dissipation is tuned only by the time step.

In the perspective of industrial applications, this presents two drawbacks that are not in our approach. Firstly, this limits the interest of implicit time advancing, since large time steps result in large spatial viscosity, and secondly this limits the possibility to really tune the numerical dissipation to a low level, since this would lead to very small time steps and then large computing effort. Conversely, in our approach, numerical dissipation can be tuned to the smallest amount required to stabilize the simulation by means of a key coefficient (γ_s). The interaction between numerical and SGS viscosities was studied *a posteriori* for both SGS models by carrying out simulations with different values of the related parameter.

In Section 2 we recall the modelling aspects; Section 3 is devoted to the description of numerical aspects. Section 4 concentrates on the presentation of the test case. Results are analysed in Section 5 and the algorithm efficiency is briefly discussed in Section 6.

2. GOVERNING EQUATIONS AND SUBGRID SCALE MODELLING

The filtered Navier–Stokes equations for a compressible Newtonian fluid are considered. The density-weighted Favre filter is introduced denoted by a ˜and defined as follows: $\tilde{f} = (\overline{\rho f})/(\bar{\rho})$, where the over-line denotes the grid filter and ρ is the density of the gas. Thus the governing equations can be written as follows:

$$\frac{\partial \bar{\rho}}{\partial t} + \frac{\partial \bar{\rho}\tilde{u}_j}{\partial x_j} = 0 \tag{1}$$

$$\frac{\partial \bar{\rho}\tilde{u}_i}{\partial t} + \frac{\partial \bar{\rho}\tilde{u}_i\tilde{u}_j}{\partial x_j} = -\frac{\partial \bar{p}}{\partial x_i} + \frac{\partial}{\partial x_j}(\mu\widetilde{P_{ij}}) - \frac{\partial M_{ij}^{(1)}}{\partial x_j} + \frac{\partial M_{ij}^{(2)}}{\partial x_j} \tag{2}$$

$$\frac{\partial \bar{\rho}\tilde{e}}{\partial t} + \frac{\partial[(\bar{\rho}\tilde{e} + \bar{p})\tilde{u}_j]}{\partial x_j} = \frac{\partial(\tilde{u}_j\mu\tilde{P}_{ij})}{\partial x_j} - \frac{\partial \tilde{q}_j}{\partial x_j} + \frac{\partial}{\partial x_j}\left(E_j^{(1)} + E_j^{(2)} + E_j^{(3)}\right) \tag{3}$$

in which μ, p, e and u_i are, respectively, viscosity, pressure, total energy and the velocity component in the i direction. The Einstein notation has been used. The tensor $\widetilde{P_{ij}}$ is defined as: $\widetilde{P_{ij}} = -\frac{2}{3}\widetilde{S_{kk}}\delta_{ij} + 2\widetilde{S_{ij}}$, in which $\widetilde{S_{ij}}$ is the resolved strain tensor,

$$\widetilde{S_{ij}} = \frac{1}{2}\left(\frac{\partial \tilde{u}_i}{\partial x_j} + \frac{\partial \tilde{u}_j}{\partial x_i}\right)$$

$\tilde{q}_j$ is the resolved heat vector flux.

The SGS model adopted here is intended to be used to study flows at high Reynolds numbers and such that low compressibility effects are present in the SGS fluctuations. In addition, we assume that heat transfer and temperature gradients are moderate.

The SGS terms in the momentum equation are:

$$M_{ij}^{(1)} = \overline{\rho u_i u_j} - \bar{\rho}\tilde{u}_i\tilde{u}_j \tag{4}$$

which is the classical SGS stress tensor, and

$$M_{ij}^{(2)} = \overline{\mu P_{ij}} - \mu\widetilde{P_{ij}} \tag{5}$$

$M_{ij}^{(2)}$ takes into account the transport of viscous terms due to small scales fluctuations. Since we are interested in high Reynolds number flows, it can be neglected compared to the SGS stress tensor, which represents the momentum transport at the SGS scales. The modelling of $M_{ij}^{(1)}$ will be described in detail in Sections 2.1 and 2.2.

The SGS terms in the energy equation are:

$$E_i^{(1)} = [\tilde{u}_i(\bar{\rho}\tilde{e} + \bar{p}) - \overline{u_i(\rho e + p)}] \tag{6}$$

$$E_i^{(2)} = \overline{\mu P_{ij} u_j} - \mu \tilde{P}_{ij} \tilde{u}_{ij} \tag{7}$$

$$E_i^{(3)} = \overline{\left(K \frac{\partial T}{\partial x_i}\right)} - \left(K \frac{\partial \tilde{T}}{\partial x_i}\right) \tag{8}$$

where K and T are, respectively, heat conductivity and temperature. The term $E_i^{(2)}$ can be neglected for high Reynolds and low Mach number flows such as those considered here. The SGS term $E_i^{(3)}$ can also be neglected under the assumption that the temperature gradients are weak in the flow, as suggested in Reference [18]. The modelling of $E_i^{(1)}$ is detailed in Sections 2.1 and 2.2.

2.1. Smagorinsky model

In order to model the SGS term $M_{ij}^{(1)}$, it is convenient to split it into its isotropic and deviatoric parts:

$$M_{ij}^{(1)} = \underbrace{M_{ij}^{(1)} - \tfrac{1}{3} M_{kk}^{(1)} \delta_{ij}}_{T_{ij}} + \underbrace{\tfrac{1}{3} M_{kk}^{(1)} \delta_{ij}}_{D_{ij}} \tag{9}$$

The deviatoric part T_{ij} can be expressed by an eddy viscosity term, in accordance with the Smagorinsky model [31] extended to compressible flows [18]:

$$T_{ij} = -\mu_{\text{sgs}} \widetilde{P_{ij}}; \quad \mu_{\text{sgs}} = \bar{\rho}(C_{\text{s}}\Delta)^2 |\tilde{S}| \tag{10}$$

in which μ_{sgs} is the SGS viscosity, Δ the filter width, C_{s} a constant that must be assigned *a priori* and $|\tilde{S}| = \sqrt{2\widetilde{S_{ij}}\widetilde{S_{ij}}}$. To complete the definition of the SGS viscosity, the grid filter width must be computed.

When an unstructured grid is used, it is not trivial to define the width of the filter corresponding to the numerical discretization. The following expression has been employed here for each grid element l:

$$\Delta^{(l)} = \max_{i=1,..,6} (\Delta_i^{(l)}) \tag{11}$$

in which $\Delta_i^{(l)}$ is the length of the ith side of the lth element. Another possible definition of Δ, already employed in LES with unstructured grids [4, 5, 9, 10], is

$$\Delta^{(l)} = \sqrt[3]{\text{Vol}(T_l)} \tag{12}$$

in which $\text{Vol}(T_l)$ is the volume of the lth tetrahedron of the mesh.

The isotropic part D_{ij} can be rewritten following Erlebacher *et al.* [32]:

$$D_{ij} = -\left(\tfrac{1}{3}\,\gamma M_{\mathrm{sgs}}^2 \bar{p}\right)\delta_{ij} \tag{13}$$

in which γ is the specific heat ratio of the flow and M_{sgs} the SGS Mach number. Since we are interested in problems for which M_{sgs} is low, D_{ij} can reasonably be neglected.

The term $E^{(1)}$ in the energy equation can be modeled in analogy with the Smagorinsky model used for the SGS tensor:

$$E_i^{(1)} = C_p \frac{\mu_{\mathrm{sgs}}}{Pr_{\mathrm{sgs}}} \frac{\partial T}{\partial x_i} \tag{14}$$

where C_p is the constant pressure specific heat. The SGS Prandtl number, Pr_{sgs}, is defined as follows: $Pr_{\mathrm{sgs}} = \mu_{\mathrm{sgs}}/K_{\mathrm{sgs}}C_p$, where K_{sgs} is the SGS heat coefficient that must be assigned *a priori*.

2.2. Dynamic model

The version of the Smagorinsky model described in the previous section is used as the base model, but the parameters $C = C_s^2$ in Equation (10) and Pr_{sgs} in Equation (14) are determined following the dynamic procedure proposed in Reference [33] and extended to compressible flows in Reference [19]. This procedure will be briefly described in the following.

A test filter of larger width than the grid one (denoted by a hat) is applied to the governing equations. Thus, a sub-test stress tensor appears in the momentum equation, which is modeled as the SGS stress tensor:

$$\mathscr{M}_{ij} = \widehat{\overline{\rho u_i u_j}} - \left(\frac{\widehat{\overline{\rho u_i}}\,\widehat{\overline{\rho u_i}}}{\hat{\bar{\rho}}}\right) = -C\hat{\Delta}^2 \hat{\bar{\rho}}|\hat{\tilde{S}}|\hat{\tilde{P}}_{ij} \tag{15}$$

where $\hat{\Delta}$ is the test filter width.

The test filter used here consists in evaluating the value of a flow variable on a given node by averaging on all the elements having this node as a vertex with a linear weighting function, which is the relative base function used in the P1 finite-element method.

It can be shown [33] that the SGS and the sub-test stress tensors are related by the following identity:

$$\mathscr{L}_{ij} = \widehat{\bar{\rho}\tilde{u}_i\tilde{u}_j} - \frac{1}{\hat{\bar{\rho}}}(\widehat{\bar{\rho}\tilde{u}_i}\,\widehat{\bar{\rho}\tilde{u}_j}) = \mathscr{M}_{ij} - \widehat{M_{ij}^{(1)}} \tag{16}$$

Then, by injecting Equations (10) and (15) in identity (16), the following tensorial equation is obtained:

$$L_{ij} = (C\Delta^2)B_{ij} \tag{17}$$

in which $L_{ij} = \mathscr{L}_{ij} - \frac{1}{3}\,\mathscr{L}_{hh}\delta_{ij}$ and

$$B_{ij} = \widehat{\bar{\rho}|\tilde{S}|\tilde{P}_{ij}} - \left(\frac{\hat{\Delta}}{\Delta}\right)^2 \hat{\bar{\rho}}|\hat{\tilde{S}}|\hat{\tilde{P}}_{ij}$$

The only unknown in Equation (17) is $C\Delta^2$ and it can be determined by a least-square method. This gives

$$(C\Delta^2) = \frac{B_{ij}L_{ij}}{B_{ij}B_{ij}} \tag{18}$$

Note that we chose to compute $C\Delta^2$ instead of C to avoid the indetermination in the definition of the filter width.

The only unknown quantity to be assigned *a priori* is the ratio $\hat{\Delta}/\Delta$. This ratio can be estimated as follows. Consistently with the definition of the test filter, at a given node *is*, $\hat{\Delta} = \sqrt[3]{\mathrm{Vol}_{is}}$ where Vol_{is} is the total volume of all the N_{is} tetrahedra having node *is* as a vertex. Similarly, one can assume that the implicit grid filter width depends on an average volume Vol_{is}/N_{is}, i.e. $\Delta = \sqrt[3]{\mathrm{Vol}_{is}/N_{is}}$. Thus, the ratio $\hat{\Delta}/\Delta$ has been defined on each node as follows:

$$\frac{\hat{\Delta}}{\Delta} = \sqrt[3]{N_{is}} \tag{19}$$

Clearly the previously discussed indetermination in the definition of the grid filter also affects the evaluation of $\hat{\Delta}/\Delta$. However, it is shown in the literature [33] that results obtained using the dynamic procedure are only moderately sensitive to variations, even large, of $\hat{\Delta}/\Delta$; thus, we expect that approximations involved in Equation (19) should be less critical than those in the definition of Δ for the Smagorinsky model.

Parameter Pr_{sgs} is computed by an analogous procedure, which is omitted here for sake of brevity. This results in

$$Pr_{\mathrm{sgs}} = \frac{\mathscr{Q}_j Z_j}{\mathscr{Q}_j \mathscr{Q}_j} \tag{20}$$

where

$$\mathscr{Q}_i = \left[(\widehat{\overline{\rho e}} + \hat{\bar{p}}) \frac{\widehat{\overline{\rho u_i}}}{\hat{\bar{\rho}}} \right] - [(\widehat{\overline{\rho e}} + \bar{p})\tilde{u}_i] \quad \text{and} \quad Z_i = C_p \left[\left(\frac{\hat{\Delta}}{\Delta} \right)^2 \hat{\bar{\rho}} |\hat{\tilde{S}}| \frac{\partial \hat{\tilde{T}}}{\partial x_j} - \left(\widehat{\bar{\rho} |\tilde{S}|} \frac{\partial \tilde{T}}{\partial x_j} \right) \right]$$

The dynamic procedure proposed in the present section is usually unstable due to the oscillating behavior of $C\Delta^2$ with negative peaks and a large auto-correlation time. In order to avoid this problem, a local smoothing is applied by averaging over neighboring grid cells. A clipping procedure is also applied, setting $C\Delta^2$ to zero when the sum of the SGS and the molecular viscosity is negative.

3. BASIC NUMERICAL INGREDIENTS

The numerical code considered herein (AERO) is a Navier–Stokes solver for Newtonian, compressible and three-dimensional flows [20]. AERO is a prototype for demonstrating innovative methods in fluid–structure interaction. It has been intensively applied to various industrial configurations (see, for instance, References [34–36]). It employs unstructured grids for description of complex moving and possibly deforming geometries. A mixed finite-volume/

finite-element method is used for space discretization. The finite-volume formulation is used for the convective terms and finite-elements for the diffusive terms.

The Roe scheme [21] represents the basic upwind component for the numerical evaluation of the convective fluxes $\mathscr{F}$:

$$\Phi^{\mathrm{R}}(W_i, W_j, \mathbf{n}) = \frac{\mathscr{F}(W_i, \mathbf{n}) + \mathscr{F}(W_j, \mathbf{n})}{2} - \gamma_s d^{\mathrm{R}}(W_i, W_j, \mathbf{n}) \tag{21}$$

$$d^{\mathrm{R}}(W_i, W_j, \mathbf{n}) = |\mathscr{R}(W_i, W_j, \mathbf{n})| \frac{W_j - W_i}{2} \tag{22}$$

in which W_i is the solution vector at the ith node, $\mathbf{n}$ is the normal to the cell boundary and $\mathscr{R}$ is the Roe Matrix.

The spatial accuracy of this scheme is only first order. The MUSCL linear reconstruction method (monotone upwind schemes for conservation laws), introduced by Van Leer [23], is therefore employed to increase the order of accuracy of the Roe scheme. The basic idea consists in expressing the Roe flux as a function of a reconstructed value of W at the boundary between the two cells centered respectively at nodes i and j: $\Phi^{\mathrm{R}}(W_{ij}, W_{ji}, \mathbf{n}_{ij})$ (see References [37, 38]). W_{ij} is extrapolated from the values of W at the nodes. This extrapolation is performed by a β-scheme:

$$\begin{cases} W_{ij} = W_i + \frac{1}{2}[(1-2\beta)(\nabla W)^{\mathrm{C}} + 2\beta(\nabla W)_i^{\mathrm{D}}]\mathbf{a}_i\mathbf{a}_j \\ W_{ji} = W_j - \frac{1}{2}[(1-2\beta)(\nabla W)^{\mathrm{C}} + 2\beta(\nabla W)_j^{\mathrm{D}}]\mathbf{a}_i\mathbf{a}_j \end{cases} \tag{23}$$

The term $(\nabla W)^{\mathrm{C}}.\mathbf{a}_i\mathbf{a}_j$ in Equation (23) is defined as

$$(\nabla W)^{\mathrm{C}}.\mathbf{a}_i\mathbf{a}_j = W_j - W_i$$

The term $(\nabla W)_i^{\mathrm{D}}$ is the so-called *nodal gradient* of W at node i, i.e. an averaging of gradients on triangles around i. When the weight β is put equal to zero, the above 'extrapolation' is in fact the interpolation resulting in a central differenced scheme, since:

$$(W_{ij})_{\beta=0} = (W_{ji})_{\beta=0} = (W_i + W_j)/2.$$

For β equal to $\frac{1}{2}$, the scheme is half-upwind, of Fromm-type, while it is equivalent to a fully upwind scheme for β equal to 1.

A classical (spatial) truncation error analysis [22] for the 1D advection model discretized by the $\beta\gamma_{\mathrm{s}}$ MUSCL scheme leads to the following equation:

$$u_t + u_x = -\frac{1}{6}(1-3\beta)u_{3x}\Delta x^2 - \frac{1}{4}\beta\gamma_{\mathrm{s}}u_{4x}\Delta x^3 + O(\Delta x^4)$$

This error analysis highlights a leading second-order dispersion error with coefficient $1/6(1-3\beta)$ and a third order dissipation error, formed of *fourth-order space derivatives*, with coefficient $1/4\beta\gamma_{\mathrm{s}}$. Note that (proof by Fourier analysis) dissipation terms formed of fourth-order space derivatives have a larger damping effect on high frequencies and a smaller effect on low frequencies than dissipation terms composed of second-order space derivatives. For $\beta = \frac{1}{3}$, the first dispersion error term vanishes and the scheme is third-order accurate; if furthermore $\gamma_{\mathrm{s}} = 0$, this scheme becomes fourth-order accurate. In this case ($\beta = \frac{1}{3}$ and $\gamma_{\mathrm{s}} = 0$),

the scheme is of centred type, and will exhibit some numerical oscillations when applied to CFD problems since the integration is co-located (by opposition to staggered or mixed elements). Our standpoint is thus to choose a small, but not vanishing value for γ_s.

Note that this analysis does not take into account either the non-linearity of the hyperbolic terms in the Navier–Stokes equations nor the possible non-uniformity of the mesh. On irregular unstructured meshes, the above scheme has shown second-order spatial accuracy, see for example Reference [39].

In practice we use β equal to $\frac{1}{3}$ in order to have a minimal dispersion. A minimal spatial dissipation is also mandatory, since, although composed of fourth-order derivatives, the spatial numerical dissipation will compete with the second derivative dissipation of the LES model and may partly deteriorate the results. In the proposed MUSCL-LES model, the pressure, as well as the other flow parameters, is stabilized by the upwinding of the scheme for a non-zero γ_s. Velocities enjoy the stabilization carried by the SGS model. Since there is no SGS term for the stabilization of pressure, the risk is that a non-physical oscillatory behavior of the pressure field may be obtained if the numerical viscosity is too low. We will therefore choose the smallest γ_s for which non-physical pressure oscillations are eliminated.

Either implicit or explicit second-order schemes can be used to advance the equations in time by a line method, i.e. time and space are treated separately. In the explicit case a Runge–Kutta algorithm is used, while in the implicit case a second-order backward differencing scheme is applied [40], which involves an explicit time derivative expressed only as a spatial residual, so that it does not depend on time step length. The resulting method is second order accurate in space and time and allows stable calculations to be carried out on very heterogeneous grids (with locally very small cells) and for a large range of Mach numbers.

For a more detailed description of the AERO code, we refer to Reference [20].

4. TEST CASE AND SIMULATION PARAMETERS

The proposed methodology is applied herein to the flow around a square cylinder at $Re = 2.2\times10^4$. This flow was investigated experimentally by Lyn and Rodi [41, 42] and data are available for the time-averaged as well as for the phase-averaged flow.

The simulations presented here were carried out with a Mach number $M = 0.1$; hence, the effects of compressibility can be neglected. The results can thus be compared with the experiments, performed for incompressible flows.

Numerical results are also available in the literature. In particular, those obtained by the contributors to a recent workshop devoted to large-eddy simulation of the same test case are documented in Reference [14]. More recent LES results are reported in References [15, 16].

The computational domain and the flow configuration considered here are represented in Figure 1. With reference to Figure 1, the domain dimensions are the following: $L_i/D = 4.5$, $L_o/D = 9.5$, $H/D = 7$, $H_z/D = 4$. They are the same as those employed by contributors to the LES workshop [14], except for a shorter distance between the cylinder and the inflow boundary L_i used here.

Two different unstructured grids, having the same number of elements (559136) and nodes (97980), but differently distributed, were used for the simulations presented here; x–y sections of the two different grids are shown in Figure 2. As can be seen, both grids are more refined in a rectangular region containing the cylinder and the wake, while outside this region the size

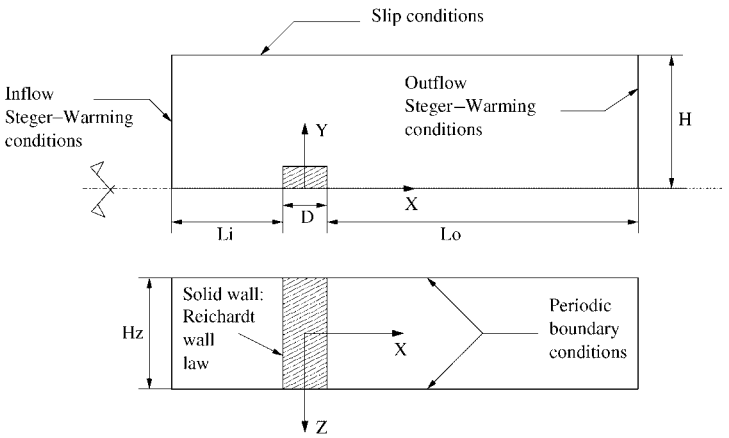

Figure 1. Computational domain.

of the elements increases progressively as the boundaries are approached. In the grid denoted GR2 this region is narrower than in the other (GR1), but it contains the same number of nodes and elements. This results in enhanced grid resolution near the cylinder and in the wake, while the elements outside the refined region are larger.

As far as the resolution in the spanwise direction is concerned, in the large-eddy simulation of the flow around a circular cylinder in Reference [19] the following rule was adopted to estimate the wavelength of the spanwise structures in the near wake:

$$\lambda_z/D \simeq 25Re^{-0.5} \tag{24}$$

which in our case gives: $\lambda_z/D \simeq 0.17$. By assuming that the rule is plausible in our case as well, approximately 32 nodes are used for both grids in the spanwise direction within the wake region, which corresponds to a spanwise resolution $\Delta z \simeq 0.125D$.

The average distance of the first layer of nodes from the cylinder surface is around $0.06D$ for GR1 and $0.02D$ for GR2. In both cases this appears to be rather large compared to near wall resolution typically used in LES. Indeed, it is estimated a posteriori that the first node is located approximately at $y^+ \in [10, 100]$ in GR1 and $y^+ \in [4, 24]$ in GR2. Approximate boundary conditions are thus assigned near the solid boundaries. In particular, a slip condition is imposed on the velocity at a distance δ from the wall. The Reichardt wall-law [17] is then used to derive the shear stresses caused by the presence of the wall. This wall law has the advantage of describing the velocity profile not only in the logarithmic region of a turbulent boundary layer ($y^+ \geqslant 40$) but also in the laminar sublayer ($y^+ \leqslant 3$) and in the intermediate region. This also guarantees correct asymptotic behaviour at the wall of the SGS terms in the Smagorinsky model.

At the inflow, the flow is assumed to be undisturbed and Steger–Warming [43] conditions are used. In Reference [16] it was shown that the introduction of a random perturbation at the inflow, corresponding to a turbulence level of about 2% as in the experiments by Lyn [41, 42], does not affect the statistics of the velocity field and the flow dynamics. Boundary conditions based on Steger–Warming decomposition are used at the outflow as well. On the side surfaces slip conditions are imposed. Finally, the flow is assumed to be periodic in the

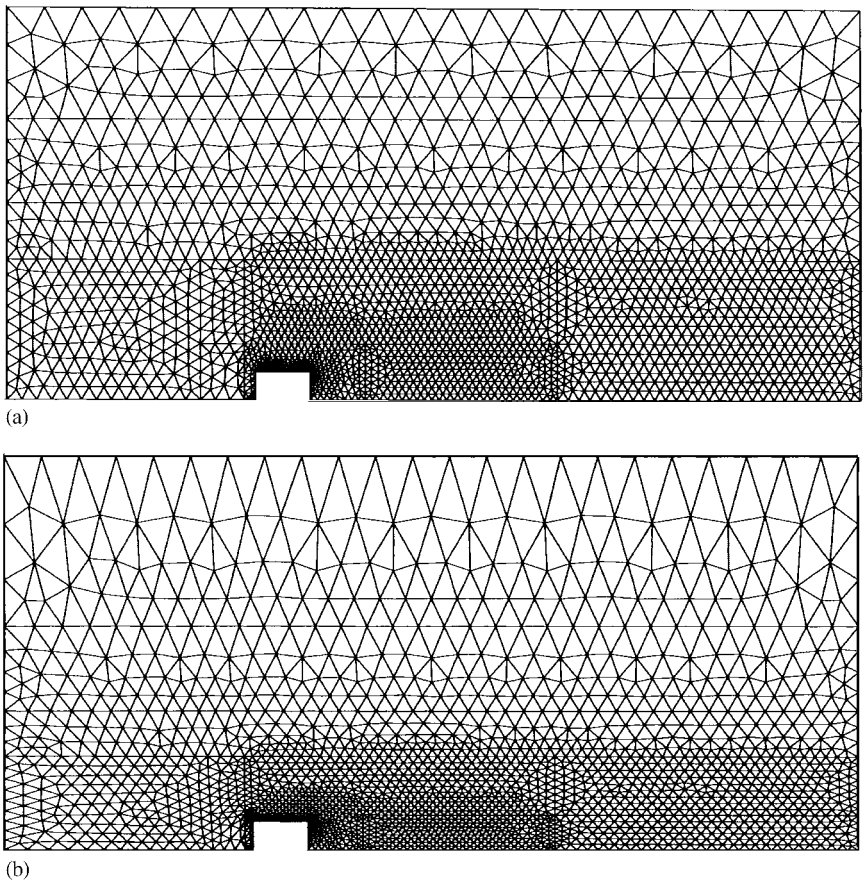

Figure 2. Computational grids; x–y section at $z = 0$: (a) GR1; (b) GR2.

spanwise direction in order to simulate a cylinder of infinite spanwise length. Note that in simulations carried out in References [14, 15] periodicity is likewise imposed in spanwise direction. Conversely, in Reference [16] semi-artificial free-slip conditions are applied on the domain boundaries normal to the spanwise direction.

Although a previous investigation [44, 45] indicated that implicit schemes and, hence, rather high values of CFL can be successfully used in LES, an explicit four-stage Runge–Kutta scheme has been used here, because periodic boundary conditions are for the moment implemented only for the explicit time advancing.

In the AERO code, parameter γ_s can be used to control the numerical viscosity of the scheme, as explained in Section 3. In previous studies [44, 45] carried out for the same test case, but with different grid and computational domain dimensions, a preliminary analysis was performed to investigate the influence of this parameter on the solutions. The Smagorinsky model was used for the SGS terms. Results indicated that numerical viscosity significantly affects the global parameters of the flow as well and that it should be reduced as far as possible in order to obtain reliable results. On the other hand, it was also shown that SGS viscosity

Table I. Main parameters in experiments and present simulations. Corrections, if present, are made to account for blockage effects (see cited references for details).

Experiments	$Re/10^4$	Blockage	Free stream turbulence (%)	Aspect ratio	End plates	Corrections
References [42, 41]	2.2	7.0	2	9.75	No	No
Reference [46]	$0.58 \div 3.2$	5.5	0.04	$\simeq 17$	Yes	No
Reference [47]	1.3	$\leqslant 5$	0.06	$\geqslant 17$	Yes	No
Reference [48]	3.4	5	0.5	9.2	Yes	Yes
Simulations	2.2	7		∞	No	No

Table II. Summary of the different simulations.

Simulation	SGS model	Grid	γ_s
SM1	Smagorinsky	GR1	0.05
SM2	Smagorinsky	GR1	0.02
SM3	Smagorinsky	GR2	0.03
DM1	Dynamic	GR1	0.10
DM2	Dynamic	GR1	0.05
DM3	Dynamic	GR2	0.06
NM1	No model	GR1	0.10

acts as a stabilizing term for the velocities and that significantly less upwinding than without SGS models is necessary. Following the above results, simulations were carried out for both Smagorinsky and dynamic SGS models and both grids with the lowest value of γ_s needed for the numerical stability of each simulation. For each model, we also present the results obtained on grid GR1 by roughly doubling the value of γ_s, in order to provide a detailed analysis of the effects on the accuracy of the results. A simulation has also been carried out on grid GR1 without any SGS model for $\gamma_s = 0.1$, which is the lowest value reachable in that case.

The results obtained in our simulations are compared with the experimental [41, 42, 46–48] and LES [14–16] data present in the literature. We also provide the results of Reference [11] as an example of RANS calculations, where the standard k–ε model and the modified k–ε model of Kato and Launder [12] are used for the closure of the equations. The main parameters of the different experiments are summarized in Table I, together with the corresponding parameters used in our simulations. Other parameters characterizing our simulations are summarized in Table II. It should be added that the constant in the Smagorinsky model was set to $C_s = 0.1$. This value is classically adopted for shear flows. As far as the dynamic model is concerned, the smoothing procedure described in Section 2.2 was used to avoid numerical instabilities. Generally, spatial averaging in homogeneous directions is used to smooth the dynamically evaluated model parameters, in order to stabilize the simulation. Even though the present test case has an homogeneous direction, it was chosen to adopt a local averaging as a smoothing procedure in order to use a general method for complex geometries, where there are usually no homogeneous directions. Procedures of local averaging of the dynamic coefficient are also used in the literature with structured grids (see, for instance, References [24, 26]). In

order to check the effects of local averaging on the results, several simulations have been performed starting from 1 smoothing cycle up to 20. The effects on the time history of the bulk coefficients were very low. In the present simulations ten smoothing cycles are used, which represent a good compromise between stability and computational cost.

5. RESULTS AND DISCUSSION

5.1. Comparison with the experiments

5.1.1. Bulk coefficients. The bulk coefficients obtained in the present simulations are shown in Table III together with the numerical and experimental results previously cited. All mean quantities presented for our simulations were evaluated by averaging in time over at least 6 shedding cycles and in the homogeneous spanwise direction. It was verified that in all cases the sample used was sufficient to obtain good statistical accuracy.

From Table III it appears that the overall agreement with the experimental data obtained in our simulations is comparable to that obtained in more resolved large-eddy simulations in the literature [14, 15].

Let us analyse now in more detail the behaviour of each parameter in Table III.

The Strouhal number is defined as

$$St = \frac{fD}{U_\infty} \tag{25}$$

where U_∞ is the free-stream velocity and f is the vortex shedding frequency evaluated in our simulations by Fourier analysis of the lift coefficient. All the experiments agree on the St value, indicating that this parameter is almost insensitive to the different experimental conditions. The sensitivity of St to SGS modelling and numerical viscosity in our simulations is low. Conversely, a significant effect of the node distribution is observed. In particular, St is predicted within experimental accuracy in all the simulations carried out on GR1 while a significant increase in St is observed on GR2 for both Smagorinsky and dynamic SGS models. This is related to the fact that, in the simulations carried out on GR2, the shear-layers detaching from the cylinder corners are less tilted with respect to the streamwise direction than in simulations on GR1, as shown for instance in Figure 3 for DM. Consequently, the frequency of vortex shedding increases.

The differences observed in the shear-layers between calculations on GR1 and GR2 also affect the value of the mean drag coefficient, which significantly decreases when GR2 is used. Simulations SM3 and DM3 should be compared with SM2 and DM2, respectively, since they are obtained with γ_s tuned in order to have the lowest amount of numerical viscosity required for the stability of each simulation. Note that, when the Smagorinsky SGS model is used, the minimum value of γ_s reachable is lower than with the dynamic model ($\gamma_s = 0.02$ in SM2 and $\gamma_s = 0.05$ in DM2, as shown in Table II). This is related to the larger SGS dissipation given by the Smagorinsky model, as discussed in further details in Section 5.2.

In all the present simulations $\overline{C_d}$ is underestimated with respect to the experimental data. Note, however, that a significant scatter is present in the experimental data as well and consequently the $\overline{C_d}$ coefficient seems to be particularly sensitive to the different experimental conditions. Likewise in our simulations, the drag coefficient was found to be significantly affected by the simulation parameters. In particular, as far as SGS modelling is concerned,

Table III. Bulk coefficients; comparison with experimental data and with other simulations described in the literature. C_l' is the r.m.s. of the lift coefficient, $\overline{C_d}$ the time-averaged drag coefficient, C_d' the r.m.s. of the drag coefficient, $-\overline{C_{pb}}$ the mean pressure coefficient at the center of the rear cylinder face, St the Strouhal number and l_r the recirculation length.

Simulations	C_l'	$\overline{C_d}$	C_d'	$-\overline{C_{pb}}$	St	l_r
SM1	0.79	1.84	0.10	1.31	0.129	1.45
SM2	0.95	1.89	0.10	1.39	0.128	1.39
SM3	0.71	1.80	0.06	1.309	0.143	1.59
DM1	0.84	1.94	0.095	1.38	0.133	1.53
DM2	0.91	2.03	0.12	1.50	0.136	1.24
DM3	0.73	1.87	0.09	1.35	0.147	1.52
NM1	0.89	1.93	0.10	1.37	0.133	1.47
Reference [14]	[0.38, 1.79]	[1.66, 2.77]	[0.10, 0.27]	—	[0.07, 0.15]	[0.89, 2.96]
Reference [15]	[1.23,1.54]	[2.03,2.32]	[0.16,0.20]	[1.3,1.63]	[0.127,0.132]	—
Reference [16]	[1.30,1.34]	[2.0,2.2]	[0.17,0.20]	—	[0.129,0.135]	[1.29,1.34]
Reference [11]	[0.05,1.17]	[1.5,2.1]	[0.002,0.068]	—	[0.122,0.146]	[1.0,3.0]
Experiments	C_l'	$\overline{C_d}$	C_d'	$-\overline{C_{pb}}$	St	l_r
References [42, 41]	—	2.1	—	—	0.132 ± 0.004	1.4
Reference [46]	1.2	2.28	—	1.6	0.13	—
Reference [47]	—	2.16	—	1.43	0.132	—
Reference [48]	1.21	2.21	0.18	1.52	0.13	—

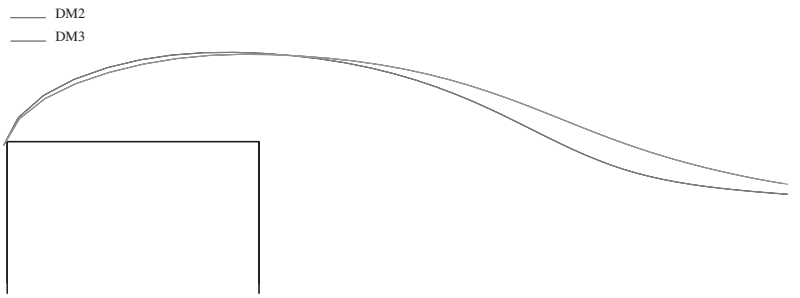

Figure 3. Streamline detaching from the cylinder corner for GR1 and GR2 (mean flow); dynamic SGS model.

the values obtained using the dynamic model are higher and in better agreement with experimental data than those given by the Smagorinsky model. An opposite trend was observed in References [14, 15] in which the Smagorinsky model seemed to systematically give higher values of $\overline{C_d}$ than the dynamic model. This difference might be related to the definition of the equivalent filter width used here for the Smagorinsky model (see Section 2.2), which leads to an excessive dissipation when the usual value for the Smagorinsky constant is used, as it is discussed in detail in Section 5.2. Furthermore, upwinding could have an appreciable influence on the SGS model behavior, especially in the case of coarse grids.

From Table III, the overall underestimate of $\overline{C_d}$ in the simulations appears to be related to the underestimate of the pressure on the rear face of the cylinder (see $-\overline{C_{pb}}$ values). However, this is not the only cause of the discrepancy, as can be seen for instance from the comparison

between computation DM2 and experiments in Reference [47]. Thus, in Reference [47] $\overline{C_d}$ is higher than in DM2 even if $-\overline{C_{pb}}$ is lower. In order to analyse the reasons for this behaviour in greater detail, the pressure coefficient distribution over the cylinder obtained in the different simulations is compared in Figure 4 with the experimental data from Reference [46] (pressure distributions from the other experiments were not available). It is evident from Figure 4(a) that in all simulations using the Smagorinsky model the absolute value of $\overline{C_p}$ is noticeably underestimated on the lateral and rear edges of the cylinder (faces BC and CD). Better agreement is found using the dynamic model, especially in the simulation on GR1 with the lowest value of numerical viscosity (DM2). More surprisingly, independently of the SGS model, the pressure coefficient is also underestimated in the front part of the cylinder (face AB), thereby explaining the underestimate of the drag coefficient even in simulations in which the base pressure is rather well predicted (see DM2). This discrepancy is caused by the inadequacy of both grids GR1 and GR2 in that region. Indeed, large elements are located too close to face AB, where gradients are high. This assumption is confirmed by the results obtained in other simulations, not reported here for sake of brevity, performed on a more refined grid, better designed in the region upwind of the cylinder. The pressure coefficient obtained in these simulations on face AB was accurately matching experimental data [49].

The r.m.s. of the lift coefficient, C_l' is available for two different experiments, which agree on its value. Conversely, it has been found to vary significantly in LES simulations in the literature [14, 15]. For RANS calculations the dispersion in C_l' is even more remarkable, and this is due to difficulties of this approach in accounting for unsteady phenomena. In particular, the standard k–ε model may give a dramatic underestimate, depending on different numerical details. In all the simulations presented here this quantity is also underestimated with respect to the experiments, although in much less extent than in k–ε RANS calculations. This discrepancy is again due to the inadequacy of both used grids in the front part of the cylinder. Indeed, values in good agreement with the experiments were obtained in the previously mentioned simulations carried out on a more refined and better designed grid [49] ($C_l' \in [1.09, 1.10], C_d' \in [0.15, 0.18]$).

The length of the recirculation bubble in the after-body (l_r) showed great variations between the different simulations in References [11, 14–16]. Our computations likewise found it to be significantly sensitive to the different simulation parameters. In particular, a decrease in numerical viscosity leads to noticeable reduction of l_r. The effect of SGS modelling is also important, but no precise trend can be identified from our simulations. As for the drag coefficient, our findings are at variance with Reference [14], in which it was observed that the dynamic SGS model gives larger l_r than the Smagorinsky model. For both SGS models, the recirculation length increases noticeably when GR2 is used. This is again related to fact that on GR2 the shear-layers detaching from the cylinder are less tilted with respect to the streamwise direction (see Figure 3).

5.1.2. Mean velocity field. Figures 5(a) and 6(a) show the streamwise distribution of U in the centre of the wake, obtained in the different simulations with SM and DM, respectively. Experimental data from References [41, 42] are also shown. The above discussed differences in recirculation length prediction are also visible in these figures. In addition, it is evident that all the simulations overestimate recovery of the streamwise velocity in the intermediate wake at about 7 diameters from the rear face. This velocity is independent of numerical viscosity

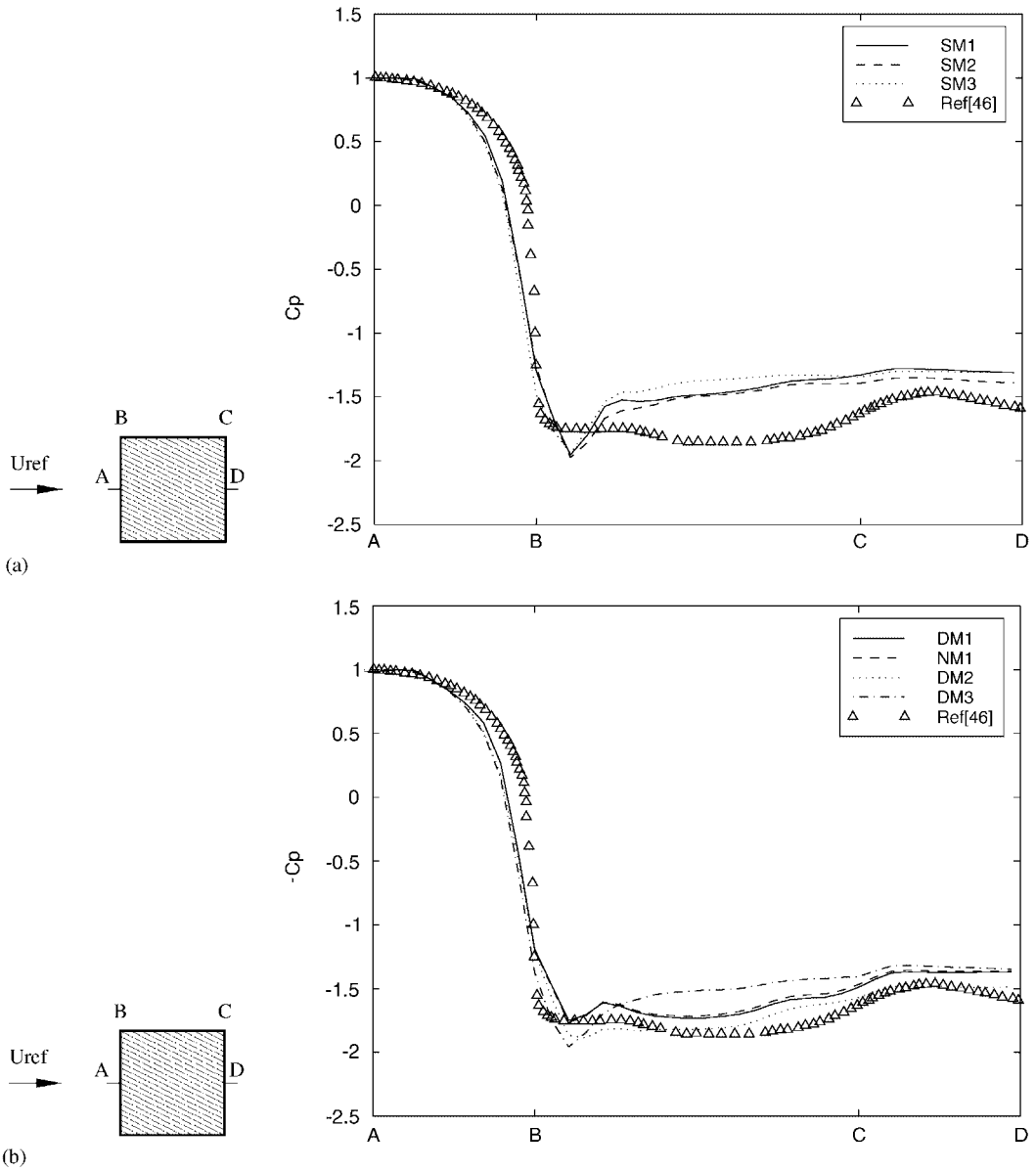

Figure 4. Numerical pressure coefficient distribution over the cylinder compared to experimental data from Reference [46]: (a) simulations with Smagorinsky SGS model; (b) simulations with dynamic SGS model and without SGS model.

and shows slight variations with SGS modelling. The effect of grid resolution is appreciable only for DM. The overestimate of the recovery velocity is a common problem for the other simulations in the literature [11, 14–16] but the reasons for this discrepancy have not yet been elucidated. In our case, the outflow boundary conditions probably have significant influence

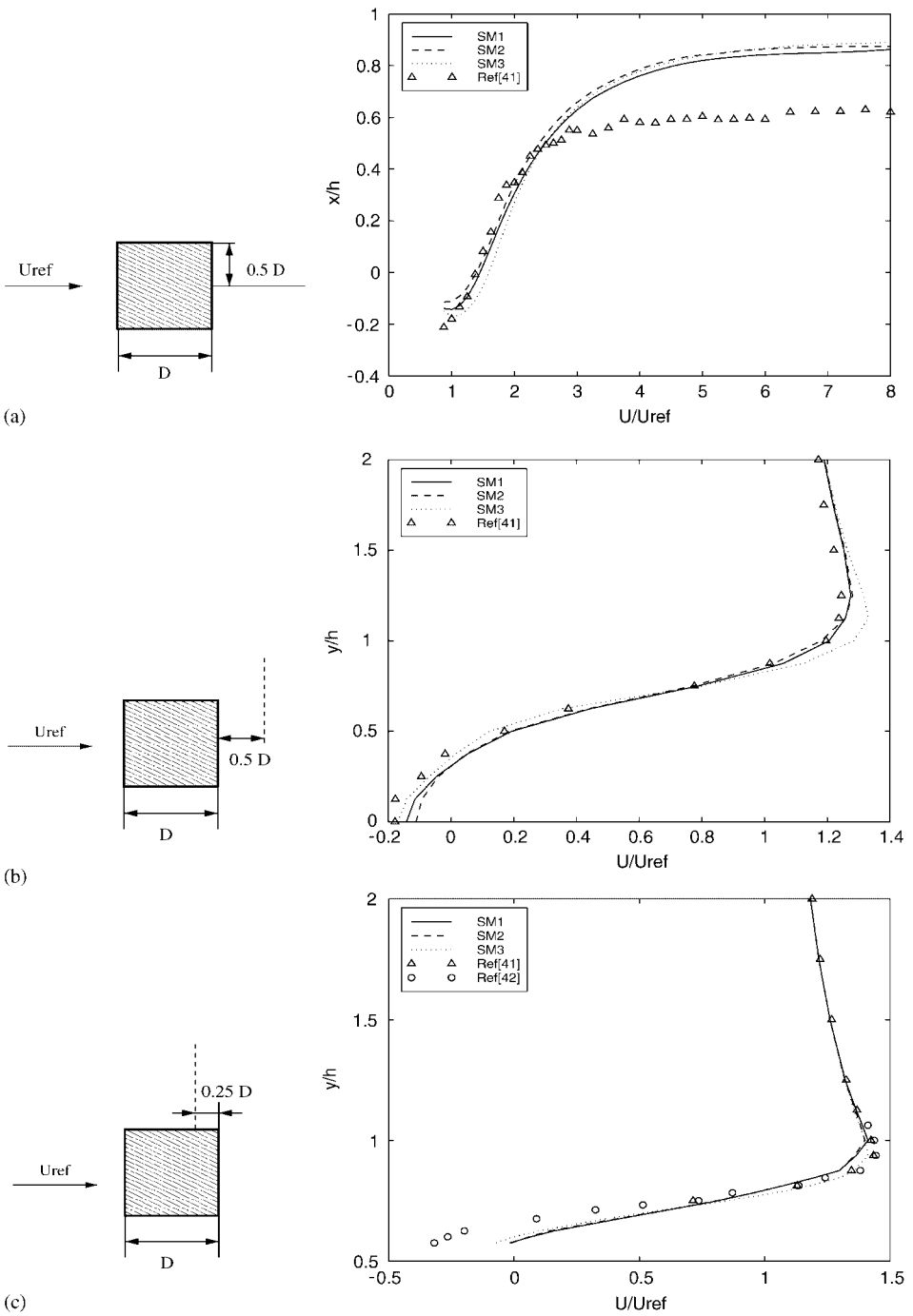

Figure 5. Mean streamwise velocity for the Smagorinsky SGS model: (a) x-distribution in the centre of the wake ($y=0$); (b) y-distribution at $x=D$; (c) y-distribution at $x=0.25D$.

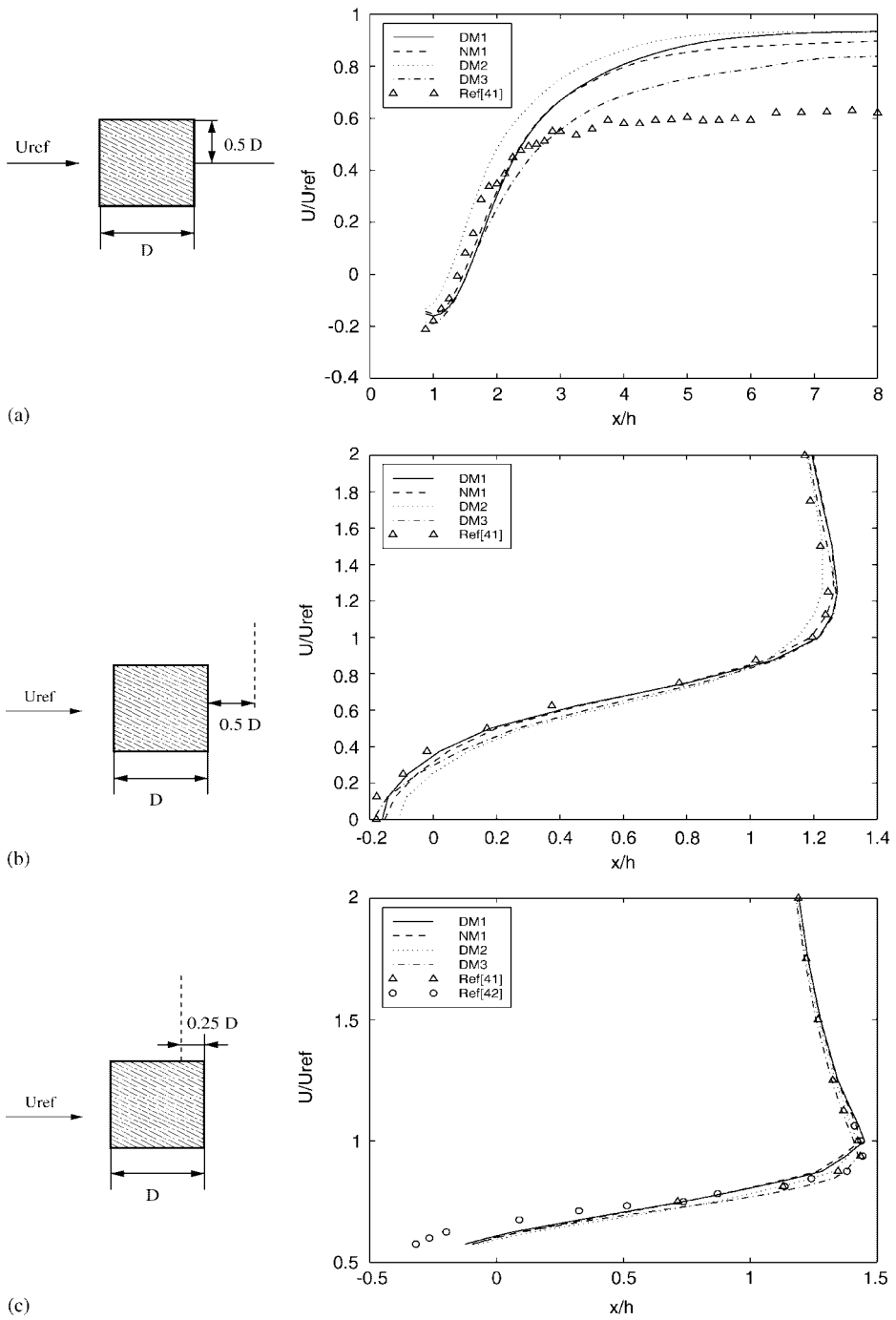

Figure 6. Mean streamwise velocity for simulations with dynamic SGS model and without SGS model: (a) x-distribution in the centre of the wake ($y = 0$); (b) y-distribution at $x = D$; (c) y-distribution at $x = 0.25D$.

on the wake region, especially on the recovery velocity, and non-reflecting conditions [50] might be more suited for this kind of flow.

Figures 5(b) and 6(b) show the profile of U in the wake at a distance of $0.5D$ from the rear face of the cylinder. The simulations employing SM and DM on GR1 fit the experimental data well; DM gives a slightly better agreement near the center line. In simulation SM3 the experimental U profile in the region $y/d \simeq 1$ is not well captured. This is probably caused by the noticeable variation in element size at that location for GR2 (see Figure 2(b)), which is particularly critical in this area where recirculating flow and strong gradients are present. This problem is not present in DM3, showing that DM seems to be less sensitive than SM to grid inhomogeneity (see also Section 5.2). This could be due to the fact that parameter $C\Delta^2$ is dynamically evaluated, instead of only C as in the classical approach, and to the smoothing procedure employed for numerical stabilization, in which $C\Delta^2$ is repeatedly averaged on neighbouring cells (see Section 2.2).

Figures 5(c) and 6(c) show the profile of U on the upper face at a distance $0.25D$ from the middle point. This profile is predicted in good agreement with the experiments in all the simulations, except for slight differences in the region close to the solid wall. However, the comparison very close to the wall is not possible since grid resolution at that section is very low.

Summarizing, for SM the numerical viscosity does not noticeably influence the mean velocity field, while the effect of grid node distribution seems to be more important. Conversely, for DM the effect of numerical viscosity seems to be the prevailing one. Following this result, we also performed a simulation (NM1 in Table II) without any SGS model and with γ_s tuned to the minimum value permitted by numerical stability ($\gamma_s = 0.1$). This value is significantly higher than for the simulations using SGS models ($\gamma_s = 0.02$ for SM and 0.05 for DM) and this confirms the fact that the SGS model has a stabilizing effect at least for the velocity. The results obtained in NM1 (see Table III and Figures 4(b), 6(a)–(c)) are very similar to those obtained with the dynamic SGS model and the same value of γ_s (DM1), confirming that in DM1 the effect of numerical viscosity was the prevailing one. However, when the dynamic model is used, the value of γ_s can be halved without encountering numerical problems (DM2) and in that case the results are significantly closer to the experimental data. This indicates that numerical viscosity cannot replace SGS modelling.

The behaviour of SGS and numerical viscosity will be analysed in further detail in the following section.

5.2. Subgrid-scale and numerical dissipation

Figure 7(a) shows the isocontours of the field $\langle \mu_{sgs}/\mu \rangle$, in which $\langle \cdot \rangle$ denotes averaging in the spanwise direction, obtained in SM1 at a time-step corresponding to a peak in the C_1 time history.

In the convective contribution to the time derivative, $\Phi^R(W_{ij}, W_{ji}, \boldsymbol{\eta}_{ij})$, the dissipation part can be separated from the central-differenced consistent advection term. The dissipation part has the following expression (Equations (21) and (22)):

$$D_{ij} = \gamma_s |\mathscr{R}| \frac{W_{ij} - W_{ji}}{2}$$

Thus we can compare the contribution to the time derivative at node i, $\mathscr{D}^{(i)} = \sum_{j \text{ neighbour } i} D_{ij}$, with that of SGS fluxes.

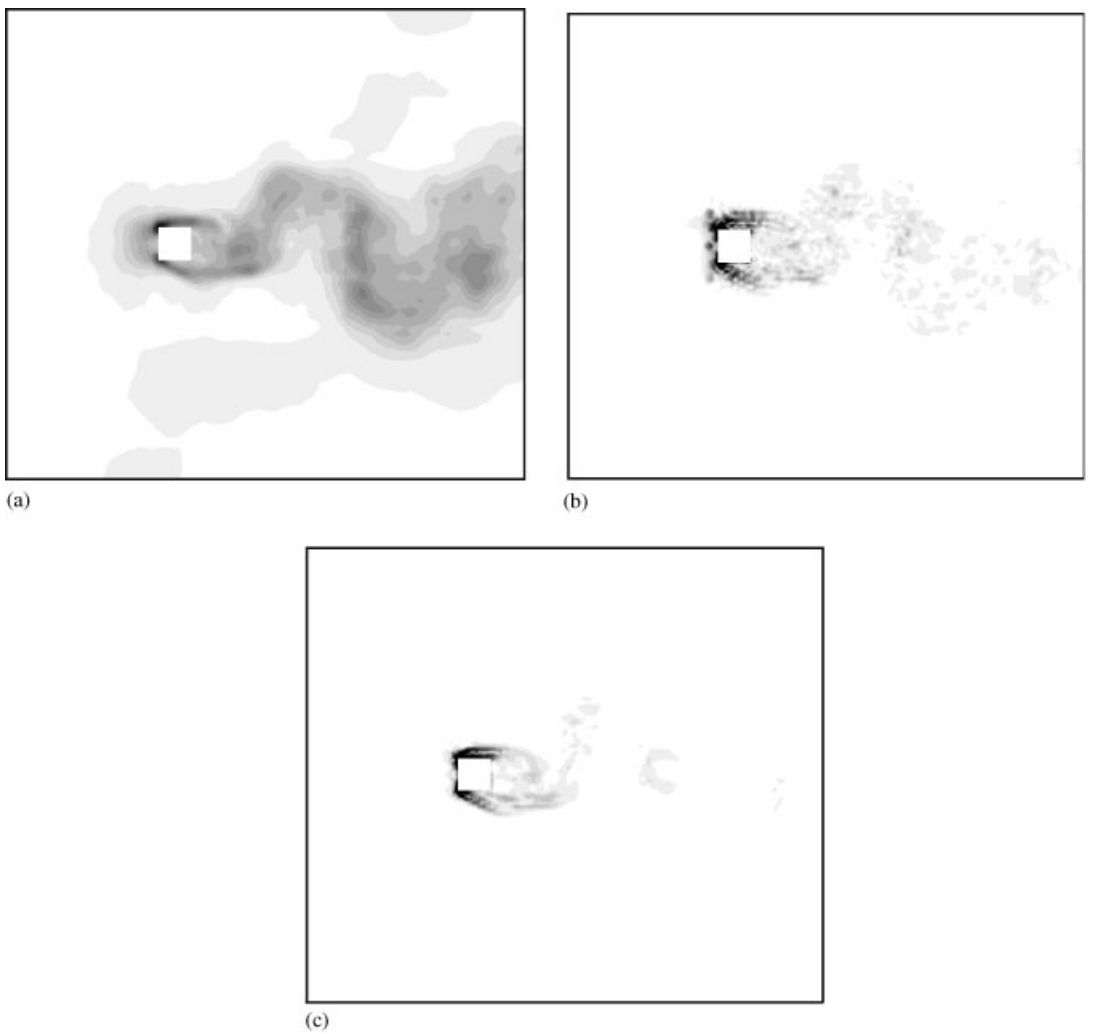

Figure 7. SM1: (a) ratio between SGS and molecular viscosity. Isocontours range from 0 (white) to 80 (black) with a step of 4; (b) norm of the upwind component of the convective flux in the momentum equation. Isocontours range from 0 (white) to 0.12 (black) with a step of 0.006; (c) norm of the SGS flux in the momentum equation. Isocontours range from 0 (white) to 0.12 (black) with a step of 0.006.

However, before discussing the comparison, two important differences between these two terms should be recalled: firstly, the $\mathscr{D}^{(i)}$ are fourth-order derivatives, which implies that their effects are more concentrated on singularities and high frequencies than the SGS second-order dissipation. Secondly, in the truncation analysis (valid only on regular meshes) the $\mathscr{D}^{(i)}$ are weighted by a coefficient $(\Delta l)^3$, while the SGS viscosity is weighted by (Δl), where Δl is the mesh size. This means that a ratio observed for a given mesh may change considerably for a slightly finer mesh.

Each component of $\mathscr{D}^{(i)}$ ($\mathscr{D}_k^{(i)}$, $k=1,5$) represents the contribution to the time derivative of each flow variable. In the following we will consider the 'norm' of $\mathscr{D}^{(i)}$, defined as

$$\|\mathscr{D}^{(i)}\| = \sqrt{\sum_{k=2}^{4} (\mathscr{D}_k^{(i)})^2}$$

Since the flow is almost incompressible, the contributions to the time derivative of density and energy will be neglected.

Figure 7(b) shows the isocontours of $\|\mathscr{D}^{(i)}\|$ obtained in SM1 at the same time-step as in Figure 7(a); isocontours of the corresponding norm of the SGS fluxes are plotted in Figure 7(c). Figures 8–10 show the same quantities as in Figure 7 for DM1, SM2 and DM2, respectively.

5.2.1. SGS model dissipation. Let us compare first Figures 7(a) with 8(a) and 9(a) with 10(a). The SGS viscosity resulting from SM is significant in the wake, in the front shear layers but also in other areas of the domain far from the body where the flow is expected to be laminar. It also shows concentrated peaks near the front edges of the cylinder. Conversely, DM gives a physically more realistic SGS viscosity field, which is significant only near the body and in the wake and has no peak near the cylinder edges. Quantitatively, the values obtained in SM and in DM are in a ratio of about 8:1. This is in contrast with previous simulations in the literature in which DM was found to give SGS viscosity peaks noticeably higher than SM. The present behaviour is probably due to the use of unstructured grids as well as to the particular definition of the filter width employed for SM. Note, in this context, that Δ_{eq} is here defined by Equation (11) instead of Equation (12), which has commonly been used in the literature. These two definitions can lead to significantly different SGS viscosity fields as the element distortion grows. *A priori* tests (not reported here for sake of brevity) showed that SGS viscosity fields obtained with Equations (11) and (12) are in a ratio of about 1 : 7 for GR1, although the two different fields are qualitatively very similar. Thus, it may be concluded that Equation (11) leads to an excessively dissipative SGS model when typical values of the Smagorinsky constant are used. Note that, in the formulation of DM used here, it is not necessary to define an equivalent filter width, Δ_{eq}, and this is an additional favorable feature besides the already known advantages of the dynamic model. Also, it has been checked that the smoothing procedure does not significantly affect the SGS viscosity field for DM.

5.2.2. SGS model versus numerics. If we now compare the upwind and the SGS fluxes (Figures 7(b), 7(c), 8(b), 8(c), 9(b), 9(c), 10(b), 10(c)) it can be noted that, independently of the SGS model used, they are qualitatively similar, even if the upwind flux is more spotty. This is consistent with the fact that numerical dissipation is expected to mainly act on the smallest resolved scales, while the effects of the SGS viscosity are significant at all the resolved scales. When SM is used, there is a ratio of about 1 : 1 between the two fluxes, indicating that the upwinding and the SGS models have a comparable effect on the solution. On the other hand, the ratio between upwinding and DM fluxes is about 1 : 10. This indicates that, when DM is used, the upwinding presumably has greater influence on the solution than the SGS model, at least on the smallest resolved scales. Note that if Equation (12) has been used for

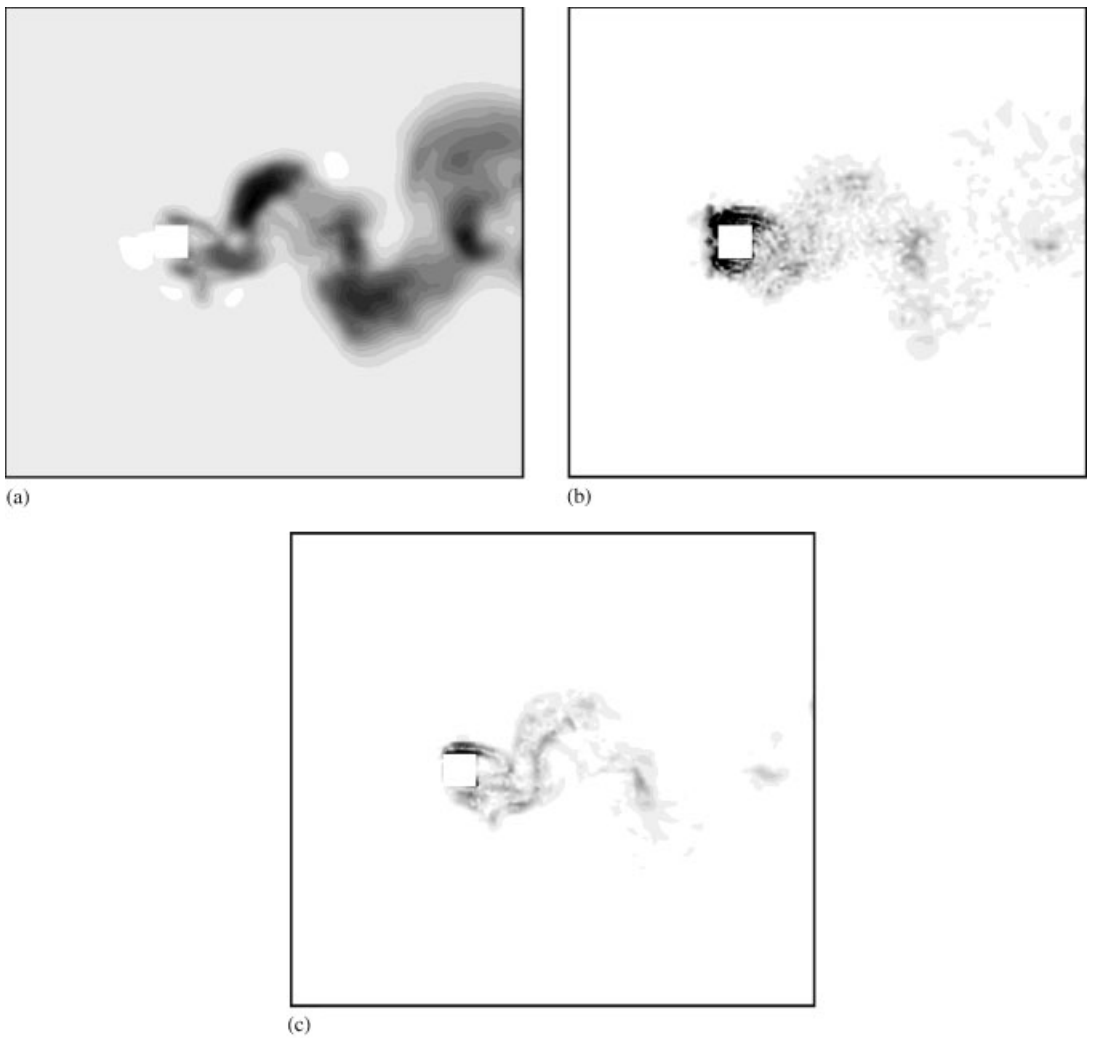

Figure 8. DM1: (a) ratio between SGS and molecular viscosity. Isocontours range from −0.55 (white) to 9.45 (black) with a step of 0.5; (b) norm of the upwind component of the convective flux in the momentum equation. Isocontours range from 0 (white) to 0.12 (black) with a step of 0.006; (c) norm of the SGS terms flux in the momentum equation. Isocontours range from 0 (white) to 0.012 (black) with a step of 0.0006.

the filter definition in SM, as discussed previously, SGS fluxes would also have been much lower than numerical upwinding.

5.2.3. Influence of node distribution. As far as the sensitivity of SGS viscosity to node distribution is concerned, Figures 11(a) and 11(b) show the ratio $\langle \mu_{sgs}/\mu \rangle$ obtained in SM3 and DM3. As expected, also on the basis of the analysis in the previous section, the Smagorinsky

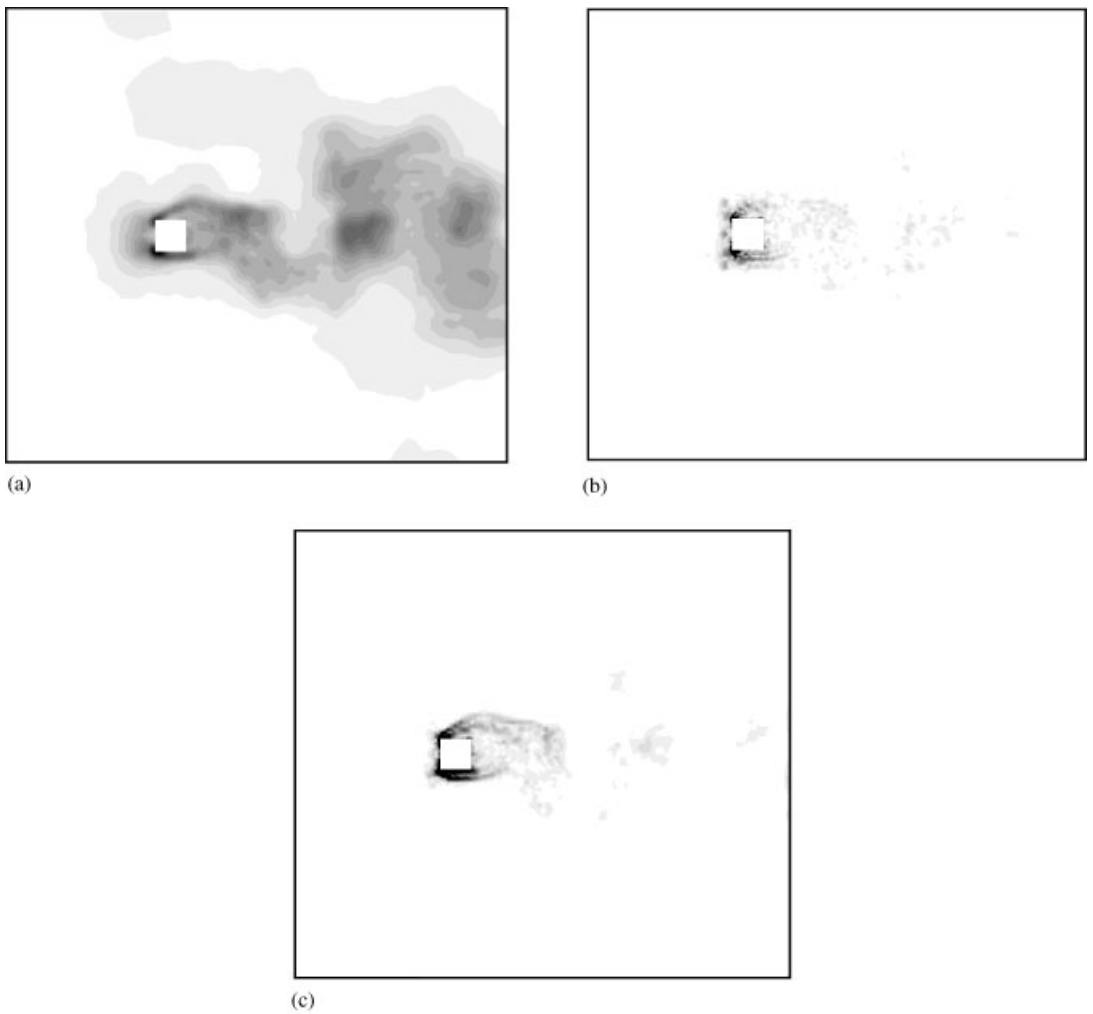

Figure 9. SM2: (a) ratio between SGS and molecular viscosity. Isocontours range from 0 (white) to 80 (black) with a step of 4; (b) norm of the upwind component of the convective flux in the momentum equation. Isocontours range from 0 (white) to 0.12 (black) with a step of 0.006; (c) norm of the SGS flux in the momentum equation. Isocontours range from 0 (white) to 0.12 (black) with a step of 0.006.

model is very sensitive to grid inhomogeneity. In particular, the problem of noticeable SGS viscosity present far from the body and the wake, where the flow is expected to be laminar, is worsened by the fact that on GR2 the size of grid elements is increased outside the refined region. This problem is eliminated with the dynamic model which gives significant SGS viscosity mainly in the wake, as in the case of GR1. However, as discussed in the previous section, grid inhomogeneity significantly affects the results also for DM.

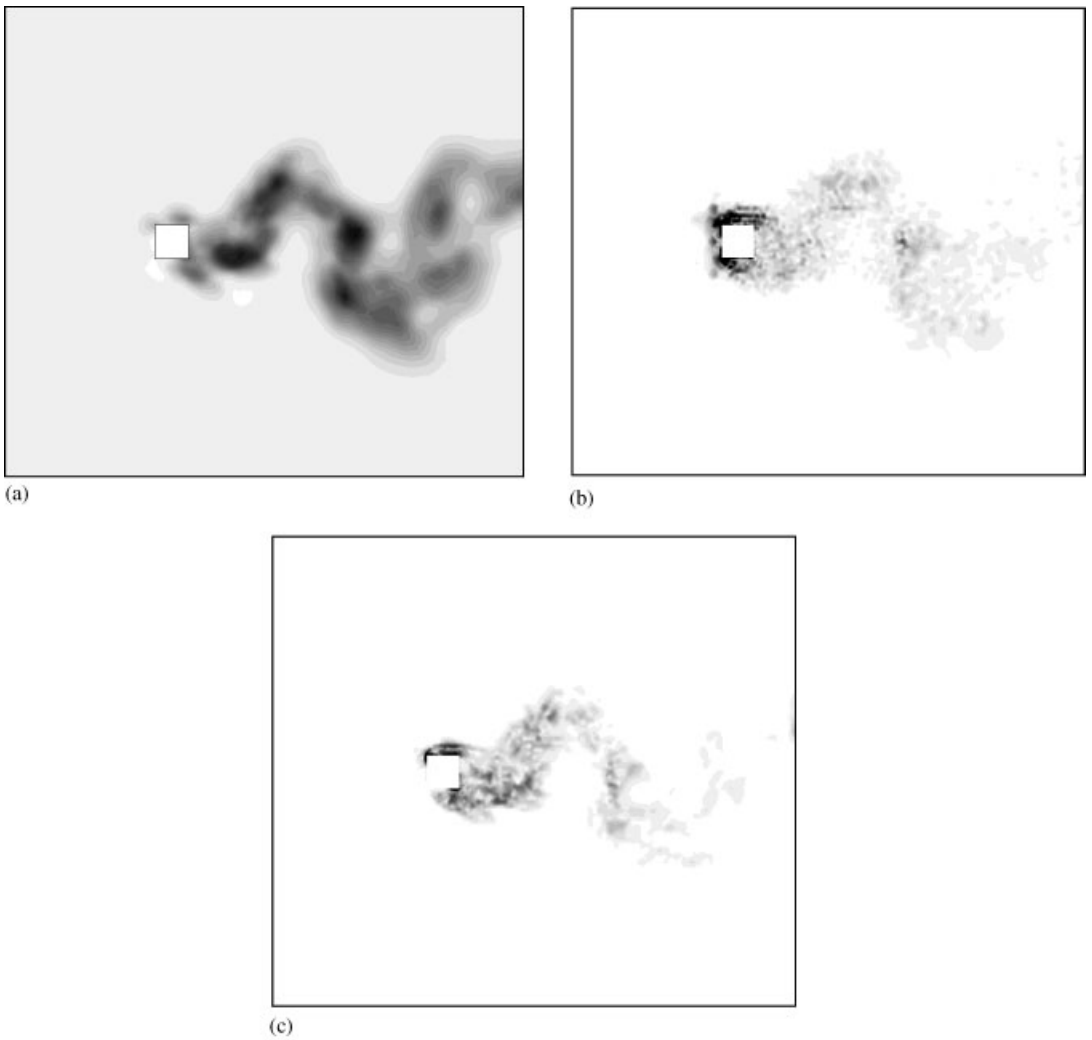

Figure 10. DM2: (a) ratio between SGS and molecular viscosity. Isocontours range from −0.55 (white) to 9.45 (black) with a step of 0.5; (b) norm of the upwind component of the convective flux in the momentum equation. Isocontours range from 0 (white) to 0.12 (black) with a step of 0.006; (c) norm of the SGS terms flux in the momentum equation. Isocontours range from 0 (white) to 0.012 (black) with a step of 0.0006.

6. ALGORITHM EFFICIENCY

The additional computational cost per time-step with respect to the laminar Navier–Stokes solution is about 13% for SM when a 4 stage Runge–Kutta procedure is used for time discretization. Note that a standard k–ε RANS model leads to an increase of approximately 30%. On the other hand, the CPU per time-step is increased by 180% for DM as the dynamic procedure on an unstructured grid requires, at each node and for each stage of the Runge–Kutta

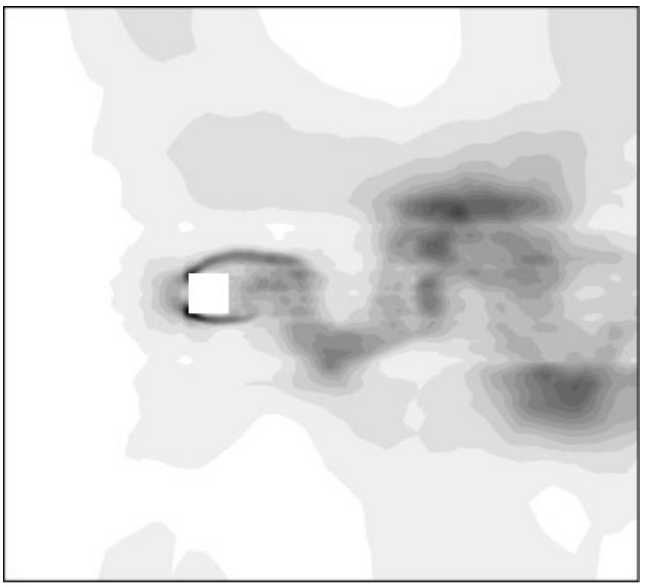

(a)

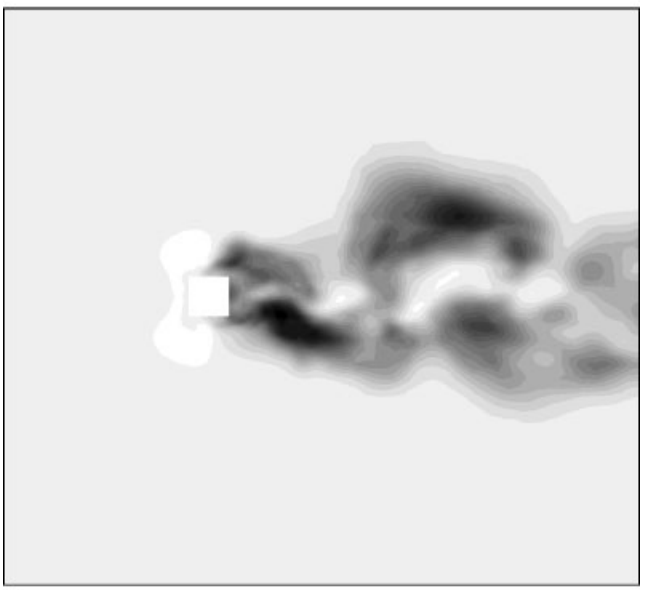

(b)

Figure 11. Ratio between SGS and molecular viscosity: (a) SM3, isocontours range from 0 (white) to 80 (black) with a step of 4; (b) DM3, isocontours range from -0.55 (white) to 9.45 (black) with a step of 0.5.

scheme, averages of several quantities over the elements containing the node (see Section 2.2). This implies a significant increase not only in CPU time, but also in memory requirements (test filtered quantities should be stored at each node). We developed an algorithm that significantly reduces the additional memory requirements but, at the same time, leads to a larger increase in CPU time. Further improvements of the algorithm in terms of CPU cost could clearly be devised. Furthermore, in order to solve the flow equations efficiently, we use a parallelization strategy which combines mesh partitioning techniques and a message-passing programming model. This strategy implies an additional communication cost for DM compared to the laminar Navier–Stokes solution, on account of the evaluation of averaged quantities at the subdomain interfaces. Note that if an implicit time advancing procedure is used, a much lower impact of SGS model computation on the global simulation cost is expected.

7. CONCLUDING REMARKS

This paper investigates the mutual adaption of an industrial CFD methodology and a LES approach. One originality of our standpoint is to propose computations with a very low level of numerical dissipation together with rather coarse and inhomogeneous meshes. This is in contrast to the use of upwinding schemes as LES models.

The numerical solver is based on a vertex centered finite-volume/finite-element formulation. Since this scheme is of co-located type, an approximate Riemann solver of Roe combined with the MUSCL interpolation is applied for spatial stability. The resulting scheme contains an upwinding parameter, γ_s, which directly controls a fourth-derivative based numerical diffusion. Two different SGS models are introduced, viz. the Smagorinsky model for compressible flows and its dynamic version.

As a first good example of the flow of interest in industry, we have applied out method to the simulation of the flow around a square cylinder at yet a low Reynolds number. Near-wall resolution requirements are relaxed by the use of approximated boundary conditions, based on a wall law.

Simulations were carried out for different values of the parameter γ_s to study the effects of numerical dissipation and its interaction with SGS terms. Sensitivity to grid inhomogeneity was also studied by using two grids having the same number of nodes, but differently distributed. Results obtained in the different simulations were compared in details with experimental data and other numerical results.

The main output of the study concerns the use of *numerical dissipation*. We have checked that if γ_s is tuned to the minimum value compatible with numerical stability, our LES calculations are of sufficient predictivity, by comparison with other LES simulations. This validates the proposed solution for the numerical stabilization of a compressible LES model.

This also validates:

— the choice of the different ingredients for the model, and in particular the utilization of the Reichardt wall law with small values of y^+,
— the use of a second-order spatial approximation on unstructured meshes,
— the application to rather coarse and inhomogeneous meshes.

The present investigation also confirms that industrial-like LES approaches are interesting for bluff-body flow simulation, at least when boundary layer separation is fixed by geometry.

However, a number of adverse results also emerge from this study.

The already known drawbacks of the Smagorinsky model are, as can be expected, more limiting when coarse and unstructured grids are used. In particular, there is as yet no theoretical work to help defining the *equivalent filter width* as a function of element size and shape on unstructured grids. We adopted a definition different from that usually employed in the literature for unstructured grids. In our simulations, Equation (11) was used instead, since it seemed more representative for the smallest resolved flow scales. However, it turned out that, for typical values of the Smagorinsky model constant, it led to an excessively dissipative SGS model. Moreover, SM is particularly sensitive to grid inhomogeneity, it is inaccurate near the flow singularities (the cylinder corners) and also gives significant dissipation far from the wake where the flow is supposed to be laminar.

The above problems are less critical for the dynamic model, especially in the formulation proposed here, in which the equivalent filter width is dynamically evaluated together with the Smagorinsky constant. For this particular flow only a few smoothing cycles were necessary at each time step to eliminate non-physical isolated peaks of SGS viscosity.

Nevertheless, for both SGS models, we encountered problems with the sensitivity of the solution to grid inhomogeneity, i.e. when large elements are close to small ones, since this is a typical situation in industrial CFD. The present study suggests that, at least for the subgrid scale models and numerical scheme employed, it is advisable to avoid abrupt changes in element size in critical areas of the flow, especially in the main convection direction.

Before the proposed method can be used for more complex flows, several lines of investigations are suggested by the present work. We discuss two of these.

As for numerics, since the present results are encouraging for the use of second-order schemes on unstructured meshes, future investigation and development should in our opinion concentrate on further pushing the logic of higher-order-derivative based diffusion towards sixth-order-derivative diffusion, as proposed in [51], in order to amplify the complementarity between the LES model and MUSCL stabilization and filtering (and further reduce their competition). In this way we also hope that the sensitivity of the results to γ_s could be reduced, thus preliminary accurate tuning of γ_s could be avoided.

As far as SGS modelling is concerned, it should be noted that, when coarse grids are used, limits of validity of eddy-viscosity models are far from having been reached. Thus, it is certainly worth testing SGS models based on different physical assumptions, such as dynamic mixed models [24, 52], deconvolution models [53] or multiscale models [54]. However, the formulation of these models on unstructured grids is not trivial and dedicated studies appear to be needed. In the perspective of application in an industrial context, it should also be assessed whether the accuracy improvement plausibly obtained with such models could compensate for the increase in computational cost (see Reference [55] for an investigation in a simple geometry with a spectral numerical scheme).

Advances in these two directions would noticeably increase the interest in extending the validation to different types of flow such as detached flows on smooth walls or higher-Reynolds flows, with the perspective of providing users with a new generation of simulation tools for unsteady aerodynamics.

REFERENCES

1. Ghosal S. An analysis of numerical errors in large-eddy simulations of turbulence. *Journal of Computational Physics* 1996; **125**(1):187–206.

2. Kravchenko AG, Moin P. Numerical studies of flow over a circular cylinder at $Re_D = 3900$. *Physics of Fluids* 2000; **12**:403–417.
3. Jansen KE. Large-eddy simulations of flow around a NACA 4412 airfoil using unstructured grids. *CTR Annual Research Briefs*, 1996.
4. Ducros F, Nicoud F, Schönfeld T. Large-eddy simulations of compressible flows on hybrid meshes. *Proceedings of the 11th Symposium Turbulent Shear Flows*, Grenoble, France, 1997; 28-1.
5. Chalot F, Marquez B, Ravachol M, Ducros F, Nicoud F, Poinsot T. A consistent finite element approach to large eddy simulation. *AIAA Paper 98-2652*, 1998.
6. Jansen KE. A stabilized finite element method for computing turbulence. *Computer Methods in Applied Mechanics and Engineering* 1999; **174**(3–4):299–317.
7. Nicoud F, Ducros F. Subgrid-scale stress modelling based on the square of the velocity gradient tensor. *Flow Turbulence and Combustion* 1999; **62**(3):183–200.
8. Colin O, Ducros F, Veynante D, Poinsot T. A thickened flame model for large-eddy simulations of turbulent premixed combustion. *Physics of Fluids* 2000; **12**:1843–1863.
9. Haworth D, Jansen KE. Large-eddy simulation on unstructured deforming meshes: towards reciprocating IC engines. *Computers and Fluids* 2000; **29**(5):493–524.
10. Okong'o N, Knight D, Zhou G. Large eddy simulations using an unstructured grid compressible Navier–Stokes algorithm. *International Journal of Computational and Fluid Dynamics* 2000; **13**:303–326.
11. Bosch G, Rodi W. Simulation of vortex shedding past a square cylinder with different turbulence models. *International Journal for Numerical Methods in Fluids* 1998; **28**:601–616.
12. Kato M, Launder BE. The modelling of turbulent flow around stationary and vibrating square cylinders. *Proceedings of the 9th Symposium Turbulent Shear Flows*, Kyoto, Japan, 1993; 10-4-1.
13. Durbin PA. Separated flow computations with the k–ε–v^2 model. *AIAA Journal* 1995; **33**(4):659–664.
14. Rodi W, Ferziger JH, Breuer M, Pourquié M. Status of large eddy simulation: results of a workshop. *ASME Journal of Fluids in Engineering* 1997; **119**:248–262.
15. Sohankar A, Davidson L, Norberg C. Large eddy simulation of flow past a square cylinder: comparison of different subgrid scale models. *ASME Journal of Fluids in Engineering* 2000; **122**:39–47.
16. Fureby C, Tabor G, Weller HG, Gosman AD. Large eddy simulation of the flow around a square prism. *AIAA Journal* 2000; **38**(3):442–452.
17. Hinze JO. *Turbulence.* McGraw-Hill: New York, 1959.
18. Lesieur M, Comte P. Large-eddy simulations of compressible turbulent flows. In *AGARD-R-819* 1997; A4.1–A4.39.
19. Moin P, Squires K, Cabot W, Lee S. A dynamic subgrid-scale model for compressible turbulence and scalar transport. *Physics of Fluids A* 1991; **3**(11):2746–2757.
20. Farhat C, Koobus B, Tran H. Simulation of vortex shedding dominated flows past rigid and flexible structures. In *Computational Methods for Fluid-Structure Interaction*, Kvamsdal T, Enevoldsen I, Herfjord KC, Jenssen B, Mehr K, and Norsett S (eds), Tapir, 1999; 1–30.
21. Roe PL. Approximate Riemann solvers, parameters, vectors and difference schemes. *Journal of Computational Physics* 1981; **43**:357–372.
22. Carpentier R. Comparison entre des schémas 2D de type Roe sur maillage régulier triangle ou quadrangle. *INRIA Report 3360*, 1998.
23. Van Leer B. Flux vector splitting for the Euler equations. *Lecture Notes in Physics*, vol. 170, 1982; 405–512.
24. Zang Y, Street RL, Koseff JR. A dynamic mixed subgrid-scale model and its application to turbulent recirculating flows. *Physics of Fluids A* 1993; **5**:3186–3196.
25. Akselvoll K, Moin P. Large-eddy simulation of turbulent confined coannular jets. *Journal of Fluid Mechanics* 1996; **315**:387–411.
26. Salvetti MV, Damiani R, Beux F. 3D coarse large-eddy simulations of the flow above two-dimensional sinusoidal waves. *International Journal for Numerical Methods in Fluids* 2001; **34**:617–642.
27. Colin O, Rudgyard M. Development of high-order Taylor–Galerkin schemes for LES. *Journal of Computational Physics* 2000; **162**:338–371.
28. Boris JP, Grinstein FF, Oran ES, Kolbe RL. New insights into large eddy simulation. *Fluid Dynamics Research* 1992; **10**:199–228.
29. Garnier E, Sagaut P, Comte P, Deville M. On the use of shock-capturing schemes for large-eddy simulation. *Journal of Computational Physics* 1999; **153**:273–311.
30. Mittal R, Moin P. Suitability of upwind-biased finite difference schemes for large-eddy simulation of turbulent flows. *AIAA Journal* 1997; **35**(8):1415–1417.
31. Smagorinsky J. General circulation experiments with the primitive equations. *Monthly Weather Review* 1963; **91**(3):99–164.
32. Erlebacher G, Hussaini MY, Speziale CG, Zang TA. Toward the large-eddy simulation of compressible flows. *Journal of Fluid Mechanics* 1992; **238**:155–185.

33. Germano M, Piomelli U, Moin P, Cabot W. A dynamic subgrid-scale eddy viscosity model. *Physics of Fluids A* 1991; **3**(7):1760–1765.
34. Lardat R, Carpentier R, Koobus B, Schall E, Dervieux A, Farhat C, Guery JF, Della Pieta P. Interaction between a pulsating flow and a perforated membrane. *Revue Européenne des Elements Finis* 2000; **9**(6–7):805–817.
35. Lardat R, Koobus B, Schall E, Dervieux A, Farhat C. Analysis of a possible coupling in a thrust inverter. *Revue Européenne des Elements Finis* 2000; **9**(6–7):819–834.
36. Schall E, Lardat R, Dervieux A, Koobus B, Farhat C. Aeroelastic coupling between a thin divergent and high pressure jets. *Revue Européenne des Elements Finis* 2000; **9**(6–7):835–851.
37. Dervieux A. Steady Euler simulations using unstructured meshes. In *Partial Differential Equations of Hyperbolic Type and Applications*, Geymonat (ed.). World Scientific: Singapore, 1987; 33–111.
38. Fezoui L, Stoufflet B. A class of implicit upwind schemes for Euler simulations with unstructured meshes. *Journal of Computational Physics* 1989; **84**:174–206.
39. Carré G, Dervieux A. On the application of FMG to variational approximation of flow problems. *Computational Fluid Dynamics Journal* 1999; **12**:99–117.
40. Martin R, Guillard H. A second-order defect correction scheme for unsteady problems. *Computers and Fluids* 1996; **25**:9–27.
41. Lyn DA, Einav S, Rodi W, Park JH. A laser-Doppler velocimeter study of ensemble-averaged characteristics of the turbulent near wake of a square cylinder. *Journal of Fluid Mechanics* 1995; **304**:285–319.
42. Lyn DA, Rodi W. The flapping shear layer formed by flow separation from the forward corner of a square cylinder. *Journal of Fluid Mechanics* 1993; **267**:353–376.
43. Steger JL, Warming RF. Flux vector splitting for the inviscid gas dynamic equations with applications to finite difference methods. *Journal of Computational Physics* 1981; **40**:263–293.
44. Camarri S, Salvetti MV. Towards the large-Eddy simulation of complex engineering flows with unstructured grids. *INRIA Report 3844*, 1999.
45. Camarri S, Koobus B, Salvetti MV, Dervieux A. Towards the large-eddy simulation of complex engineering flows. In *Proceedings of ECCOMAS 2000*, European Congress on Computational Methods in Applied Sciences and Engineering, 11–14 September 2000, Barcelona (Spain).
46. Bearman PW, Obasaju ED. An experimental study of pressure fluctuations on fixed and oscillating square-section cylinders. *Journal of Fluid Mechanics* 1981; **119**:297–321.
47. Norberg C. Flow around rectangular cylinders: pressure forces and wake frequencies. *Journal of Wind Engineering and Industrial Aerodynamics* 1993; **49**:187–196.
48. Luo SC, Yazdani MdG, Chew YT, Lee TS. Effects of incidence and afterbody shape on flow past bluff cylinders. *Journal of Industrial Aerodynamics* 1994; **53**:375–399.
49. Camarri S, Koobus B, Salvetti MV, Dervieux A. Low diffusion MUSCL schemes for LES on unstructured grids. *INRIA Report* 4515, 2002.
50. Poinsot TJ, Lele SK. Boundary conditions for direct simulations of compressible viscous flows. *Journal of Computational Physics* 1992; **101**:104–129.
51. Debiez C, Dervieux A. Mixed element volume MUSCL methods with weak viscosity for steady and unsteady flow calculation. *Computers and Fluids* 2000; **29**:89–118.
52. Salvetti MV, Banerjee S. A priori tests of a new dynamic subgrid-scale model for finite-difference large-eddy simulations. *Physics of Fluids* 1995; **7**:2831–2847.
53. Domaradzki JA, Saiki EM. A subgrid-scale model based on the estimation of unresolved scales of turbulence. *Physics of Fluids* 1997; **9**:2148–2164.
54. Hughes TJR, Mazzei L, Jansen KE. Large eddy simulation and the variational multiscale method. *Computers in Visual Science* 2000; **3**:47–59.
55. Sarghini F, Piomelli U, Balaras E. Scale-similar models for large-eddy simulations. *Physics of Fluids* 1999; **11**: 1596–1607.

